Precision measurement of the oscillator strength of the cesium $6\,^2S_{1/2} \rightarrow 5\,^2D_{5/2}$ electric quadrupole transition in propagating and evanescent wave fields

Satoshi Tojo,* Takashi Fujimoto, and Masahiro Hasuo

Department of Engineering Physics and Mechanics, Graduate School of Engineering, Kyoto University, Kyoto 606-8501, Japan

(Received 5 February 2004; revised manuscript received 4 August 2004; published 31 January 2005)

Hyperfine-structure-resolved absorption spectra of the $6\,^2S_{1/2} \rightarrow 5\,^2D_{5/2}$ of cesium atoms have been observed with a temperature-controlled cell and a diode laser. From a comparison with the absorption of the D_2 transition at the same atom density range, the oscillator strength of the electric quadrupole transition was determined to be $(4.69\pm0.05)\times10^{-7}$. Reflection spectra of the same transition have also been observed in the partial and total reflection regimes with a reflection cell. An increase in the apparent oscillator strength was observed for total reflection with an increase in the angle of incidence, by a factor up to 1.5 at θ_c +83.8 mrad and 2.4 at θ_c+107.5 mrad for s and p polarizations, respectively, where θ_c is the critical angle. The observed enhancement is ascribed to the incidence-angle-dependent wave vector and polarization vector of the evanescent wave.

I. INTRODUCTION

The oscillator strength of the electric quadrupole transition ($6\,^2S_{1/2} \rightarrow n\,^2D_{5/2,3/2}$) of cesium atoms was determined by various methods in the 1960s and 1970s as shown in Table I [1–8]: e.g., by the light absorption method, by the hook method by use of anomalous dispersion, and by the two-photon ionization method. For the $6\,^2S_{1/2} - 5\,^2D_{5/2}$ transition the experimental values of the oscillator strength range from 4.43×10^{-7} to 1.85×10^{-6}. Theoretical calculations give smaller values of $(4.37-4.60)\times10^{-7}$ [6,9]. All of these values are with the hyperfine structure (HFS) components unresolved.

The recent development of diode laser techniques made a quantitative absorption observation possible even for weak absorption lines and therefore a determination of the oscillator strength of an electric quadrupole transition. The accuracy of the oscillator strength directly depends on that of the atom density in the measurement. Since the oscillator strengths of the D lines of cesium atoms ($6S$–$6P$) are well determined, the oscillator strength of the electric quadrupole transition can be determined from a comparison of the absorption intensities of the D lines and the electric quadrupole transitions measured under the same atom density.

The above development also made it possible to observe reflection spectra of weak transitions. The oscillator strength of an electric quadrupole transition from the initial state $|i\rangle$ to the final state $|f\rangle$ is proportional to $|\hat{\mathbf{e}}\cdot\langle f|\mathsf{Q}|i\rangle\cdot\mathbf{k}|^2$, where $\hat{\mathbf{e}}$ is the unit polarization vector of the light, Q is the quadrupole tensor, and $\mathbf{k}$ is the wave vector of the light [10]. Since the wave and polarization vectors of the evanescent (inhomogeneous) wave are different from those of the propagating (homogeneous) wave in free space owing to the spatial localization of the light field, the magnitude of the oscillator strength may be modified in the evanescent wave field. Recently, such

modifications were actually observed in attenuated total reflection (ATR) spectroscopy [11].

In this article, we present a detailed report of the precision measurement of the electric quadrupole transition by absorption and reflection spectroscopy.

II. DETERMINATION OF THE OSCILLATOR STRENGTH BY ABSORPTION SPECTROSCOPY

A. Experimental setup

Figure 1(a) shows the experimental arrangement which consists of the setup for the absorption measurement of the $6\,^2S_{1/2} \rightarrow 6\,^2P_{3/2}$ electric dipole transition (the D_2 transition, 852.11 nm) and that of the $6\,^2S_{1/2} \rightarrow 5\,^2D_{5/2}$ electric quadrupole transition (684.89 nm). Figure 1(b) shows the energy-level diagram of the respective transitions [12].

For the D_2 transition measurement we use a tungsten filament lamp with a current of 1.2 A. The light from the lamp is made approximately parallel by a lens and goes through a cylindrical Pyrex-glass absorption cell in which cesium atoms are sealed. The absorption cell has a 100-mm-long optical path length and a 20-mm-long leg connected to the side wall of the cell body. The coldest point, which determines the cesium vapor pressure, is on the leg of the cell. The temperature at the coldest point is controlled in the range from 293.1 ± 0.1 to 470.7 ± 0.2 K and the main body is kept at a slightly higher temperature than the coldest point temperature. The heater wires are wound around the cell in such a way that the induced magnetic fields almost cancel in it. We monitor the electromotive force of three thermocouples on the main body to keep the temperature uniform.

The light that passes through the cell is focused on the entrance slit of the spectrometer (1 m focal length). The spectrometer has a 1200-groove/mm grating and a 24-μm entrance slit. The linear reciprocal dispersion near the D_2 transition is calibrated with the emission lines from an argon discharge lamp to be $0.023\,786+9.091\,44\times10^3\lambda$, where λ is the wavelength in meters. A color glass filter (Optima,

* Present address: Department of Physics, Graduate School of Science, Kyoto University, Kyoto 606-8502, Japan.

TABLE I. The oscillator strength of the Cs $6\,^2S_{1/2} \to 5\,^2D_{5/2}$ transition.

Author	Value (10^{-7})	Density (m^{-3})	Method	Year
Shrum et al.[a]		(Unspecified)	Emission spectroscopy	1927
Prokofíev[b]	18.5	$\approx 10^{23}$	Hook method	1929
Gridneva and Kasobov[c]	17.7	4.9×10^{21}	Emission spectroscopy	1965
Warner[d]	4.37		Theory (Coulomb approximation)	1968
Hertel and Ross[e]	17.6	(Unspecified)	Electron impact technique	1969
Sayer et al.[f]	5.07	10^{21}–3×10^{22}	Absorption spectroscopy	1971
	4.60		Theory (Coulomb approximation)	1971
Exton[g]	5.46	(Unspecified)	Absorption spectroscopy	1976
Niemax[h]	5.65 ± 0.28	10^{21}–5×10^{23}	Absorption spectroscopy	1977
Glab and Nayfeh[i]	4.43 ± 0.32	$\approx 10^{14}$	Two-photon ionization with buffer gas by pulsed laser	1981
This work	4.69 ± 0.05	8.91×10^{19}–1.46×10^{21}	Absorption spectroscopy by cw laser	2004
($F=4 \to F'$)	4.69 ± 0.06			
($F=3 \to F'$)	4.68 ± 0.06			

[a]Reference [1].
[b]Reference [3].
[c]Reference [4].
[d]Reference [9].
[e]Reference [5]. They observed it in an unresolved $6\,^2S_{1/2} \to 5\,^2D_{3/2,5/2}$ transition.
[f]Reference [6].
[g]Reference [7].
[h]Reference [2].
[i]Reference [8].

JB450), which cuts light of wavelength below 430 nm, is placed in front of the slit to eliminate the higher-order diffracted light. A liquid-nitrogen-cooled charge-coupled device (CCD) camera (Princeton Instruments, CCD-1100PF) is located on the focal plane of the spectrometer. The size of the pixel is 24×24 μm. The exposure time is 20 s.

For the absorption measurement of the electric quadrupole transition, we use an external-cavity diode laser (EOSI, Model 2010) of the output power up to 6 mW and the spectral linewidth of 1 MHz at the wavelength of 685 nm. The laser light frequency is tuned by the voltage applied to the piezoelectric element of the external cavity. The sinusoidal voltage from a function generator (Iwatsu, SG-4111) is superimposed on the sweeping voltage for the purpose of laser light frequency modulation. The modulation frequency is 1 kHz. The modulation amplitudes are 30.1 ± 0.2 MHz near the $F=4 \to F'=2,3,4,5,6$ transitions and 32.4 ± 0.1 MHz near the $F=3 \to F'=1,2,3,4,5$ transitions, respectively.

After passing through an optical isolator (Isowave, I-6070-CM), a part of the laser beam is incident on a wavemeter (Burleigh Instrument, WA4500D) for the light frequency monitor. Another portion of the laser beam is led to a Fabry-Pérot interferometer (Tropel, Model 216). The free spectral range is 299.2 ± 0.2 MHz. The output of the interferometer is used as a frequency marker. The main part of the laser beam goes through a half-wave plate and a Glan-Thompson prism, which are used for adjustment of the laser light intensity. After going through a 0.5-mm-diameter aperture, a part of the laser beam power is detected by a photodiode (Hamamatsu, S1336-5KB) as the light intensity reference. The laser beam is incident onto the absorption cell. The intensity of the laser light is 0.19 mW/mm^2 and the transmitted laser light is detected by another photodiode. The signal of the photodiode is lock-in amplified (Princeton Applied Research, Model 5204) with respect to the frequency modulation. The output of the lock-in amplifier is registered by a digital recorder (Keyence, Waveshot 2000) together with the direct output of the photodiode, the light intensity reference, and the frequency marker.

B. Results and discussion

Figure 2(a) shows examples of the transmission spectra measured for the D_2 transition. The HFS in both the upper and lower states is unresolved in any spectrum because the spectral resolution of 6.627 GHz determined by the pixel size of the CCD camera is insufficient to separate the HFS splitting of the lower state, 9.193 GHz. We made a measurement with the heater current cut off just before the measurement. No appreciable change was detected. Thus, we eliminated possible effects by the magnetic field induced by the heater current.

For a measure of the absorption intensity, we calculate the equivalent width defined as

$$W_\nu = \int_{\text{line}} [1 - T(\nu)] d\nu, \tag{1}$$

where $T(\nu)$ is the transmission spectrum. This width is independent of the spectral resolution of a spectrometer and equal to that calculated from the absorption coefficient $K(\nu)$ as

$$W_\nu = \int_{\text{line}} \{1 - \exp[-K(\nu)l]\} d\nu, \tag{2}$$

where l is the absorption length. The absorption coefficient is given as $K(\nu) = 2\pi\nu \, \text{Im}[\chi(\nu)]/[c\,\eta(\nu)]$, where c is the speed
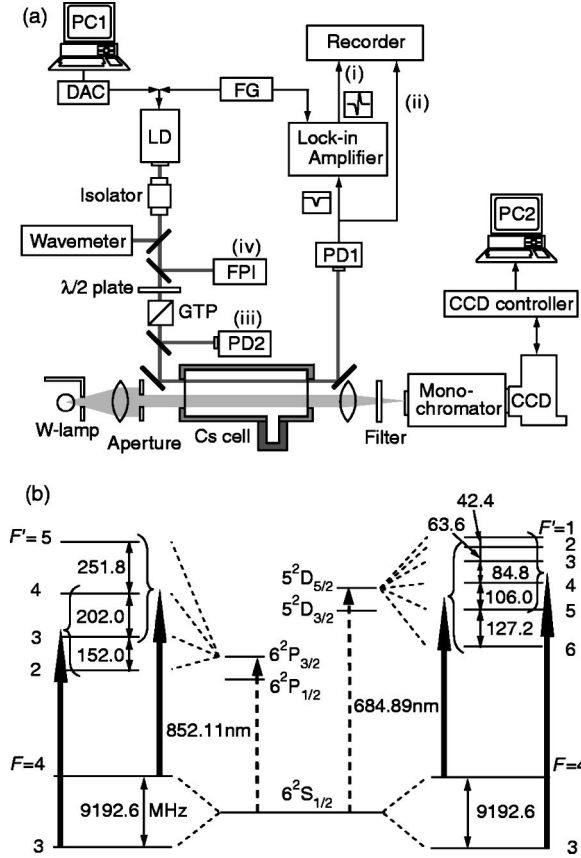
FIG. 1. (a) The experimental setup. LD, laser diode; FPI, Fabry-Pérot interferometer; PD, photodiode; GTP, Glan-Thompson prism; FG, function generator; DAC, digital-analog converter; W-lamp, tungsten filament lamp; CCD, CCD camera. (b) Energy-level diagrams of the Cs $6\,^2S_{1/2} \rightarrow 6\,^2P_{3/2}$ (left) and $6\,^2S_{1/2} \rightarrow 5\,^2D_{5/2}$ (right) transitions with the HFS splitting.

of light in vacuum. $\eta(\nu)$ and $\chi(\nu)$ are the real part of the refractive index and the electric susceptibility of the atomic vapor, respectively.

In the case where the difference of $\eta(\nu)$ from unity is negligibly small, which is the case in our experimental condition, we can approximate the absorption coefficient to be

$$
\begin{aligned}
K(\nu) &= \frac{2\pi\nu}{c}\mathrm{Im}[\chi(\nu)] \\
&= \frac{Ne^2\sqrt{\ln 2}}{2\pi^{3/2}\epsilon_0 m_e c\Delta_G}\sum_{F',F}\int_0^\infty \frac{f^{F',F}\frac{1}{2}\Gamma_L}{(\nu'-\nu)^2+\left(\frac{1}{2}\Gamma_L\right)^2} \\
&\quad \times \exp\left[-4\ln 2\left(\frac{\nu'-\nu_{F',F}}{\Delta_G}\right)^2\right]d\nu',
\end{aligned}
\tag{3}
$$

where N is the atom density in the vapor, e is the elementary charge, ϵ_0 is the dielectric constant of vacuum, m_e is the electron mass, F' and F are the total angular momentum quantum numbers of the upper and lower HFS states, respectively, $\nu_{F',F}$ is the resonance frequency of the transition from F to F', $f^{F',F}$ is the relevant oscillator strength, Δ_G is the
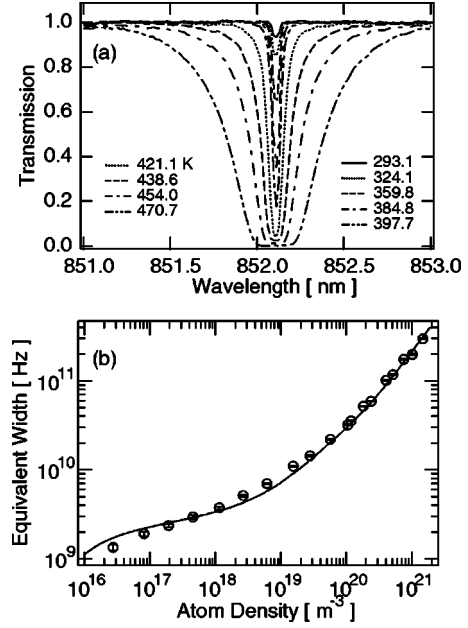

FIG. 2. (a) Transmission spectra of the $6\,^2S_{1/2} \rightarrow 6\,^2P_{3/2}$ electric dipole transition at several temperatures of the coldest point. (b) The dependence of the equivalent width on the atom density; the experiment (open circles) and the calculation (solid line).

Gaussian width (the Doppler width), and Γ_L is the Lorentzian width.

The oscillator strength of an electric dipole transition is distributed over the HFS states from that in the fine structure scheme according to the relation [13]

$$
f_D^{F',F} = (2F+1)(2F'+1)\left\{\begin{matrix} J & I & F \\ F' & 1 & J' \end{matrix}\right\}^2 f_D,
\tag{4}
$$

where L,L' and S,S' are the orbital and spin angular momentum quantum numbers, J,J' are the angular momentum quantum numbers of the fine structure, I is the nuclear spin angular momentum quantum numbers, and $\{\}$ is the 6-j symbol. Here, $J=1/2$, $J'=3/2$, and $I=9/2$. The oscillator strength f_D is expressed as

$$
f_D = \frac{4\pi m_e \nu_0}{g\hbar}\sum_m |\langle f|\mathbf{r}|i\rangle|^2,
\tag{5}
$$

where m shows a magnetic sublevel of the final state, ν_0 is the resonance frequency between the initial and the final states, and g is the statistical weight of the initial state [14,15].

We calculate the equivalent width of the D_2 transition with the HFS splittings included. The oscillator strength is 0.7149 [16]. The Lorentzian width includes the resonance collision broadening $\gamma_{\mathrm{coll}}=(1.15\pm0.12)\times10^{-13}N$ Hz [17]. The solid curve in Fig. 2(b) is the calculated equivalent width as a function of the atom density. The open circles in the figure show the experimental results. In this case, the atom density is evaluated from the temperatures of the cell body and the coldest point with the empirical vapor pressure against the coldest point temperature [18]. A reasonable agreement between calculation and experiment is seen,
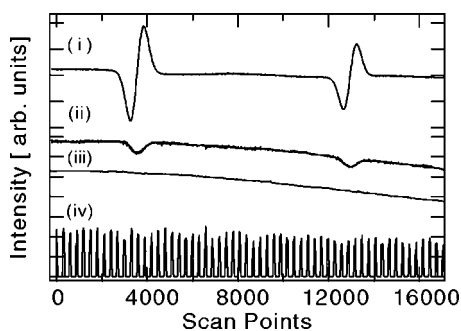
FIG. 3. An example of raw data for the transmission spectra measurement of the $6\,^2S_{1/2} \rightarrow 5\,^2D_{5/2}$ electric quadrupole transition. The temperatures of the coldest point and the main body of the cell are 470.7 and 477.5 K, respectively. (i) The lock-in amplified signal of the laser light intensity transmitted through the cell, (ii) the transmitted light intensity, (iii) the light intensity reference, and (iv) the frequency marker. (i), (ii), (iii), and (iv) correspond to those in Fig. 1(a).

which suggests that the relation between the vapor pressure and the coldest point temperature is reasonable and that the present temperature measurement is adequate. However, since the difference between experiment and calculation in the atom density reaches 20% in the high-density region of the experiment, we determine the atom density not from the temperatures of the cell but from the measured equivalent width for the determination of the oscillator strength of the electric quadrupole transition.

Figure 3 shows an example of the raw data for the measurement of the electric quadrupole transition. The temperatures of the coldest point and the main body of the cell are 470.7 and 477.5 K, respectively. The atom density evaluated from the equivalent width of the D_2 transition is $N=1.42 \times 10^{21}$ m^{-3}. The Lorentzian width Γ_L is determined by the lifetime of the $5\,^2D_{5/2}$ state to be 129.8 kHz [19] because the resonance collision broadening of the electric quadrupole transition is negligibly small; it is of the order of 100 Hz. Due to the frequency modulation, the spectrum of the output from the lock-in amplifier is the first derivative of the transmission spectrum. When we changed the intensity of the incident laser light from 0.02 to 0.30 mW/mm², no appreciable difference was observed in the spectra in any respect except for statistical fluctuations. Thus, our experiment was confirmed to be free from any saturation effect. We also confirmed no possible effects by the magnetic field induced by the heater current. The two structures in Fig. 3 correspond to the HFS splitting of the ground state $6\,^2S_{1/2}$. The splittings of the upper levels are too small to be separated in the present experiment owing to the Doppler width of 594.1 MHz at 477.5 K. By using the traces (i) and (ii) we calibrate the gain of our system. The scan points are converted into the light frequency detuning with the use of the frequency marker.

The solid curves in Fig. 4 are the transmission spectra (the first derivative) thus calibrated. The dashed curves in the figure are calculated ones from Eq. (3). Here the oscillator strength of the electric quadrupole transition is given as [14,15]
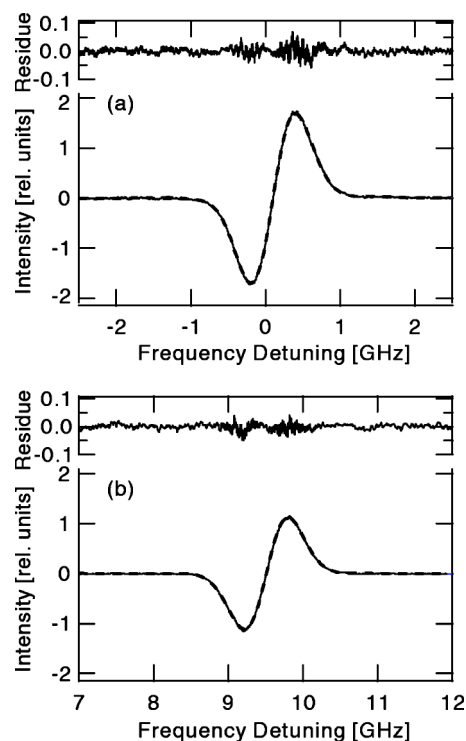

FIG. 4. The absorption spectra (the first derivative) for (a) $6\,^2S_{1/2}(F=4) \rightarrow 5\,^2D_{5/2}(F'=2\text{–}6)$ and (b) $6\,^2S_{1/2}(F=3) \rightarrow 5\,^2D_{5/2}(F'=1\text{–}5)$ transitions. The temperatures of the coldest point and the main body are 445.5 and 462.3 K, respectively. The density is 5.319×10^{20} m^{-3}. The solid and dashed curves show the experimental and calculated results, respectively.

$$f_Q = \frac{\pi m_e \nu_0}{g\hbar} \sum_m |\hat{\mathbf{e}} \cdot \langle f|Q|i\rangle \cdot \mathbf{k}|^2. \qquad (6)$$

The oscillator strength is distributed over the HFS states from that in the fine structure scheme according to the relation

$$f_Q^{F',F} = (2F+1)(2F'+1) \begin{Bmatrix} J & I & F \\ F' & 2 & J' \end{Bmatrix}^2 f_Q. \qquad (7)$$

Here, $J' = 5/2$. In the calculation we convolute the theoretical spectrum with the experimental function. Excellent agreement between the calculation and the experiment is seen in Fig. 4 and the residue is very small. Both spectra are found to be asymmetric owing to the asymmetric HFS [Fig. 1(b)]. If we fit the spectrum with a single Gaussian function, the residue increases greatly by a factor of 5 at the maximum. Thus, we clearly observed the effect of the HFS splittings of the upper level in the spectra.

Figure 5 shows the oscillator strength evaluated at several atom densities. The dominant part of the uncertainty σ comes from that in the density determination from the equivalent width (0.93σ). Other factors are due to the detector noise (0.34σ), the uncertainty in the modulation amplitude (0.10σ), and the fitting accuracy (0.06σ). We determine the overall uncertainty by following the error propagation procedure. Taking the average, we determine the oscillator
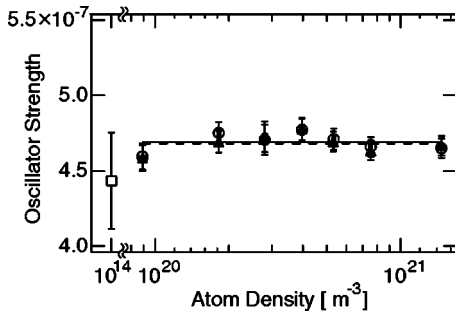
FIG. 5. The oscillator strength determined at several atom densities. For the $6\,^2S_{1/2}(F=4) \rightarrow 5\,^2D_{5/2}(F'=2-6)$ transition, the experimental values are shown by the closed circles and the fitted value is shown by the solid line. For the $6\,^2S_{1/2}(F=3) \rightarrow 5\,^2D_{5/2}(F'=1-5)$ transition, the experimental values are shown by the closed triangles The experimental value by Glab (open square) [8] is also shown.

strength f_Q to be $(4.69 \pm 0.06) \times 10^{-7}$ for the $6\,^2S_{1/2}(F=4) \rightarrow 5\,^2D_{5/2}(F'=2,3,4,5,6)$ transition and to be $(4.68 \pm 0.06) \times 10^{-7}$ for the $6\,^2S_{1/2}(F=3) \rightarrow 5\,^2D_{5/2}(F'=1,2,3,4,5)$ transition. These values are shown in Table I. The result agrees with the experimental value of Ref. [8] and the theoretical value of Ref. [6] within experimental uncertainties. Other experiments give larger values. In these latter experiments, rather high atom densities were used for the purpose of obtaining sufficient signal intensities. In a high-density vapor, even the molecular density would be substantial ($>10^{18}$ m^{-3}). In this case, the collision-induced dipole transition could enhance the electric quadrupole transition; this enhancement is due to the wave function mixing induced by collisions [20], and may result in larger values of the observed oscillator strength.

III. OBSERVATION OF THE OSCILLATOR STRENGTH ENHANCEMENT IN THE EVANESCENT LIGHT FIELD

A. Experimental setup

Figure 6(a) shows the experimental arrangement. The light source is the same diode laser as in the absorption measurement. We also adopt the frequency modulation technique. The modulation frequency is 1 kHz. The modulation amplitudes are 65.9 ± 0.4 MHz for the $6\,^2S_{1/2}(F=4) \rightarrow 5\,^2D_{5/2}(F'=2,3,4,5,6)$ transition and 74.6 ± 0.2 MHz for the $6\,^2S_{1/2}(F=3) \rightarrow 5\,^2D_{5/2}(F'=1,2,3,4,5)$. After passing through the optical isolator a part of the laser beam is incident on a Fabry-Pérot interferometer (Nihon Kagaku Eng., SA40C). The interferometer is used as a frequency marker and its free spectral range is 1.870 ± 0.007 GHz. The main part of the laser sbeam goes through a half-wave plate in order to rotate the polarization direction of the light. By a Glan-Thompson prism, the polarization of the laser light is made horizontal (p polarization) or vertical (s polarization). The intensity of the laser light is controlled by adjustment of the optical axis of the half-wave plate.

Figure 6(b) is the schematic illustration of the reflection cell (Arte Glass Associates Co., Ltd.). A half of the main part
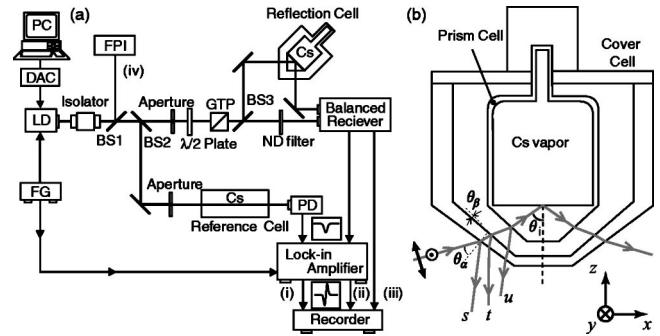

FIG. 6. (a) The experimental setup. LD, laser diode; FPI, Fabry-Pérot interferometer; GTP, Glan-Thompson prism; PD, photodiode; FG, function generator; DAC, digital-analog converter; BS, beam splitter. (b) The geometry of the reflection cell which includes the prism cell and the cover cell.

of the laser light is incident on the reflection cell which includes the prism cell and the cover cell. A drop of cesium was sealed in the prism cell under 10^{-6} Torr of vacuum. The main body of the prism cell and the leg (20 mm long) on the opposite side to the prism, which are covered by a cover cell, are heated independently, so that the temperature of the main body is uniform and the leg served as the coldest point. Throughout the measurement, temperatures of the leg and the main body of the cell are kept at 560 and 603 K, respectively. The heater wires are wound in such a way that the induced magnetic fields almost cancel in the cell.

Alkali-metal atoms tend to contaminate and corrode the surface of the cell made of glass, and the degree of erosion depends on the atom density. The prism cell is made of special quartz (Tosoh Quartz Corp.) which is synthesized by the vapor-phase axial deposition method to reduce its erosion at high atom density. The refractive index is 1.456 at 685 nm, giving the critical angle $\theta_c = 0.7571$ rad (43.38 °) for total reflection.

We determine the angle of incidence θ_i from a schematic location of the prism cell. Figure 6(b) shows the light paths through the cover cell and the prism. The window of the cover cell is wedged by 1° so as to eliminate the interference between the reflected light from the outer and inner surfaces. Let the angle of incidence on the outer surface of the cover cell window be θ_α, the relative angle between the inner surface of the window and the prism for internal reflection be θ_β, and the angle of incidence on the inner surface of the prism be θ_i. The observed relationships among the reflected light rays indicated by s, t, and u in Fig. 6(b) are used for the purpose of determining θ_β and aligning the prism cell and the cover cell. When the path of the reflected ray from the surface of the prism cell coincides with the incident ray, this indicates that the basic angle of the prism is $\pi/2$ rad and the angle of incidence θ_i is $\pi/4$ rad (45°). We can determine θ_i from the direction of the reflected ray u with respect to its direction at $\theta_i = \pi/4$. The accuracy of this method is 1.1 mrad (0.06°), which is limited by the spatial accuracy of the ray u. In addition to this method, we determine relative angles from θ_c with high precision by the ATR spectra whose profiles dramatically change near θ_c as described later. The overall accuracy could be improved to be 0.3 mrad (0.02°). We con-
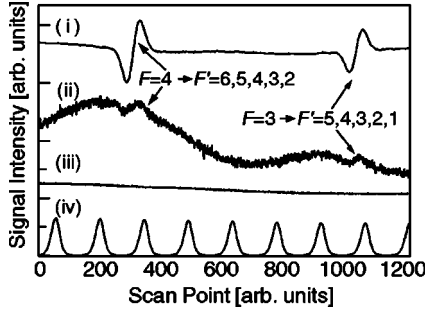
FIG. 7. An example of raw data of the ATR spectroscopy on the $6\,^2S_{1/2} \rightarrow 5\,^2D_{5/2}$ transition. (i) The lock-in amplified signal of the transmitted light through the reference cell, (ii) that of the reflected light by the prism cell, (iii) the laser light intensity, and (iv) the frequency marker. θ_i is 0.7571 rad (43.38°).

trol θ_i in the range from $\theta_c - (11.9 \pm 0.3)$ to $\theta_c + (107.5 \pm 0.3)$ mrad.

The reflected light and the other half of the main part of the laser light are detected by a balanced detector (New Focus, 2007M Nirvana Receiver). The output is lock-in amplified at the modulation frequency by the lock-in amplifier.

Another part of the laser light goes through the precise absorption cell. The transmitted light is detected and the output is also lock-in amplified. The temperature of the cell is 382 K at the coldest point, corresponding to the net atom density 2.46×10^{19} m^{-3}[18]. The transmission spectrum is used as the frequency standard for the reflection spectrum measured simultaneously.

B. Results and discussion

Figure 7 shows an example of the raw data of the lock-in amplified signals for the reference absorption cell (i) and the prism cell (ii) together with the laser light intensity monitor from the balanced detector (iii) and the frequency marker (iv). The two structures indicated by the arrows in Fig. 7 correspond to the HFS splitting of the ground state $6\,^2S_{1/2}$ in Figs. 1(b) and 3. The splittings of the upper levels are too small to be resolved in the spectrum owing to the Doppler width of 660 MHz at 590 K. We confirmed that our experiment was free from any saturation effect and possible effects caused by the magnetic field induced by the heater current. In Fig. 7 the absorption signal (ii) is superposed by undulations, which are ascribed to optical interference in the optics. We eliminated the latter by subtracting sine curves from the raw data. With the laser light intensity [curve (iii) in Fig. 7] we calibrated the gain of our system. The scan points are converted into light frequency detuning with the frequency marker. Hereafter, we concentrate on the spectra in the $F = 4 \rightarrow F'$ transition because the signal-to-noise ratios in this transition are higher than those in the $F = 3 \rightarrow F'$ transition.

The solid curves in Fig. 8 show examples of the reflection spectra (a) and (b) for $\theta_i < \theta_c$ (partial reflection), and (c), (d), (e), and (f) for $\theta_i > \theta_c$ (total reflection) for s and p polarizations. Each spectrum is the first derivative of the reflection spectrum owing to the frequency modulation. Figures 8(a), 8(c), and 8(e) are for s polarization and the result of averag-
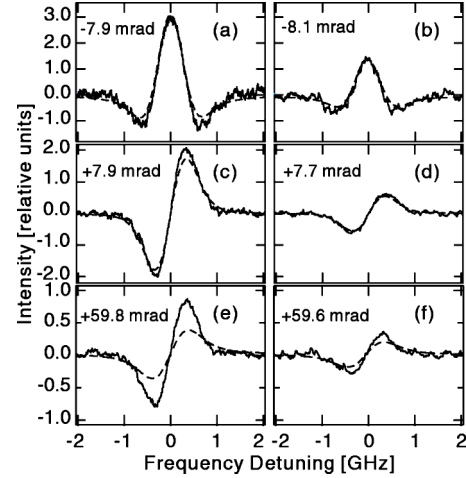

FIG. 8. Comparison of the experimental spectrum (solid line) with the calculated one (dotted line) in which the oscillator strength is assumed to be constant; (a),(c),(e) for p polarization and (b),(d),(f) for s polarization. The angular detuning is shown in each figure.

ing over 3, 10, and 17 scans, respectively. In the case of Fig. 8(c), the peak absorption is estimated to be 6.13×10^{-5} of the incidence light intensity. The solid curves in Fig. 8(b), 8(d), and 8(f), are for p polarization, which are the result of averaging over 5, 5, and 21 scans, respectively. For partial reflection ($\theta_i < \theta_c$) the observed signal is obviously the first derivative of a dispersion-type spectrum, while for $\theta_i > \theta_c$ that of an absorption-type spectrum is seen.

The reflection spectra for both partial and total reflection are given from the Fresnel formulas as

$$\mathcal{R}_s(\nu) = \left| \frac{n_1 \cos \theta_i - \sqrt{n_2(\nu)^2 - n_1^2 \sin^2 \theta_i}}{n_1 \cos \theta_i + \sqrt{n_2(\nu)^2 - n_1^2 \sin^2 \theta_i}} \right|^2, \quad (8)$$

$$\mathcal{R}_p(\nu) = \left| \frac{n_1 \cos \theta_i - [n_1/n_2(\nu)]^2 \sqrt{n_2(\nu)^2 - n_1^2 \sin^2 \theta_i}}{n_1 \cos \theta_i + [n_1/n_2(\nu)]^2 \sqrt{n_2(\nu)^2 - n_1^2 \sin^2 \theta_i}} \right|^2, \quad (9)$$

for s and p polarizations, respectively. Here n_1 and $n_2(\nu)$ are the refractive index of the dielectric medium and that of the atomic vapor, respectively. The refractive index of the atomic vapor is related to its electric susceptibility as $n_2(\nu) = \sqrt{1 + \chi(\nu)}$.

For total reflection, there is no longer a flow of energy across the boundary in the absence of absorption by the atoms, even though the electromagnetic field is present in the atomic vapor. This evanescent field gives rise to the absorption in ATR and has the inhomogeneous wave vector, the x and z components of which are given as

$$k_x = k_0 n_1 \sin \theta_i, \quad (10)$$

$$k_z = i k_0 \sqrt{n_1^2 \sin^2 \theta_i - n_2^2}. \quad (11)$$

Here, we define the x axis along the direction parallel to the surface in the plane of incidence and the z axis in the direc-

tion normal to the surface. For ATR, the electric susceptibility of the atomic vapor is given as [21,22]

$$\chi(\nu) = \frac{Ne^2 \sqrt{\ln 2}}{4\pi^3 \epsilon_0 m_e \nu_0 w \Delta_G(k_x/k_0)}$$
$$\times \sum_{F',F} \int_{-\infty}^{\infty} \int_0^{\infty} \frac{f^{F',F}}{\nu' - \nu - i\left[\frac{1}{2}\Gamma_L - ik_z v_z\right]}$$
$$\times \exp\left[-4\ln 2\left(\frac{\nu' - \nu_{F',F}}{\Delta_G(k_x/k_0)}\right)^2\right] \exp\left[-\left(\frac{v_z}{w}\right)^2\right] d\nu' dv_z,$$

(12)

where w is the mean velocity of the atoms. The factor of k_x/k_0 in the Doppler broadening is due to the parallel component of the wave vector of the evanescent light to the boundary; this wave vector is larger than that of the propagating light wave. The additional term in the broadening of the Lorentzian function $-ik_z v_z$ is the transit-time broadening for an atom in the vapor traveling through the evanescent light field, which decays exponentially in the z direction with the decay constant of i/k_z [21]. Since the decay constant, which is called the penetration depth of the evanescent field, is about the light wavelength, the effect of the transit-time broadening is substantial.

From Eqs. (8) and (9) the reflection spectra for an optically thin vapor, which is the case of our experimental condition, i.e., $|\chi(\nu)| < 3.78 \times 10^{-6} \ll 1$ at the maximum, are approximated to be

$$\mathcal{R}_s(\nu) = 1 - \frac{4n_1 \cos\theta_i}{n_1^2 \cos^2\theta_i + (n_1^2 \sin^2\theta_i - 1)} \frac{\text{Im}[\chi(\nu)]}{2\sqrt{n_1^2 \sin^2\theta_i - 1}},$$

(13)

$$\mathcal{R}_p(\nu) = 1 - \frac{4n_1 \cos\theta_i(2n_1^2 \sin^2\theta_i - 1)}{\cos^2\theta_i + n_1^2(n_1^2 \sin^2\theta_i - 1)} \frac{\text{Im}[\chi(\nu)]}{2\sqrt{n_1^2 \sin^2\theta_i - 1}},$$

(14)

for s and p polarizations, respectively. In this case, the observed spectra originate from the second terms in the right-hand sides of Eqs. (13) and (14), which are proportional to $\text{Im}[\chi(\nu)]$ with a θ_i-dependent proportionality factor for the respective polarizations. The ratio of the factor for p polarization to that for s polarization near θ_c is n_1^2 (~ 2.1), which accounts for the signal intensity ratio between Figs. 8(c) and 8(d). Since the broadening of the signal spectrum depends on θ_i, we define here the equivalent width, which is free from the broadening as

$$A_{s,p}^{\text{total}}(\nu) = \int_{\text{line}} [1 - R_{s,p}^{\text{total}}(\nu)] d\nu.$$

(15)

This value is proportional to the θ_i-dependent proportionality factor and the oscillator strength.

For partial reflection, the electric susceptibility is free from the effects of the pseudomomentum and the transit-time broadening and given as [21]

$$\chi(\nu) = \frac{Ne^2 \sqrt{\ln 2}}{4\pi^{5/2} \epsilon_0 m_e \nu_0 \Delta_G} \sum_{F',F} \int_0^{\infty} \frac{f^{F',F}}{\nu' - \nu - i\frac{1}{2}\Gamma_L}$$
$$\times \exp\left[-4\ln 2\left(\frac{\nu' - \nu_{F',F}}{\Delta_G}\right)^2\right] d\nu'.$$

(16)

When the atomic vapor is optically thin, the reflection spectra are approximated to be expressed as

$$\mathcal{R}_s(\nu) = 1 - \frac{4n_1 \cos\theta_i \sqrt{1 - n_1^2 \sin^2\theta_i}}{|n_1 \cos\theta_i + \sqrt{1 - n_1^2 \sin^2\theta_i}|^2}$$
$$+ \frac{4n_1 \cos\theta_i \, \text{Re}[\chi(\nu)]}{2\sqrt{1 - n_1^2 \sin^2\theta_i}|n_1 \cos\theta_i + \sqrt{1 - n_1^2 \sin^2\theta_i}|^2},$$

(17)

$$\mathcal{R}_p(\nu) = 1 - \frac{4n_1 \cos\theta_i \sqrt{1 - n_1^2 \sin^2\theta_i}}{|\cos\theta_i + n_1 \sqrt{1 - n_1^2 \sin^2\theta_i}|^2}$$
$$+ \frac{4n_1 \cos\theta_i(3 - 2n_1^2 \sin^2\theta_i) \, \text{Re}[\chi(\nu)]}{2\sqrt{1 - n_1^2 \sin^2\theta_i}|\cos\theta_i + n_1 \sqrt{1 - n_1^2 \sin^2\theta_i}|^2},$$

(18)

for s and p polarizations, respectively. Therefore, the observed spectra originate from the third terms on the right-hand sides of Eqs. (17) and (18), which are proportional to $\text{Re}[\chi(\nu)]$ with corresponding θ_i-dependent proportionality factors. Similar to the case of total reflection the ratio of the factor for p polarization to that for s polarization near θ_c is n_1^2, which accounts for the signal intensity ratio between Figs. 8(a) and 8(b). We define the quantity $A_{s,p}^{\text{partial}}(\theta_i)$, which corresponds to the equivalent width in the ATR spectra, from the peak-to-peak intensity of the derivative signal and the linewidth of the dispersion type reflection spectrum.

Since the determination of the absolute angle of incidence with high precision is difficult in the experiment, we determine the angular detuning $\delta = \theta_i - \theta_c$ as follows. Near the critical angle, the θ_i-dependent proportionality factors for both the partial and total reflections are proportional to $1/|\delta|^{1/2}$ under the condition of $|\chi| \ll |\delta| \ll 1$ [23,24]. We determine θ_c by fitting $1/|\delta|^{1/2}$ curves to the angular dependence of $A_{s,p}(\theta_i)$, and then we determine δ [11]. In Fig. 8, the determined values of δ are shown. The slight difference in δ between s and p polarizations, 0.2 mrad, is caused by the slightly different laser paths owing to the rotation of the Glan-Thompson prism for switching the polarization direction.

The accuracy of the atom density estimated from the coldest point temperature is not clear at such a high temperature. We fit the measured partial reflection spectra with the first derivative of the theoretical spectrum using the value of f_Q determined in Sec. II. The atom density obtained by averaging over the fitted results for measured partial reflection spectra is 2.15×10^{22} m^3. The value is about 20% larger than that evaluated from the coldest point temperature with the empirical relation [18]. The discrepancy is within the accuracy of the atom density, which is seen in Fig. 2(b). No
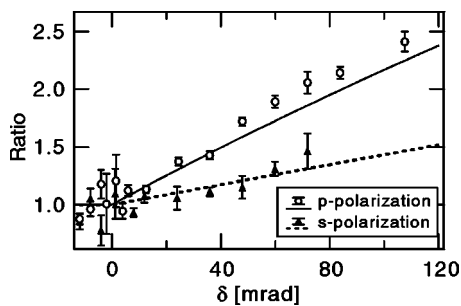
FIG. 9. The ratio of $A_{s;p}(\theta_i)$ between experiment and calculation, as a function of the angular detuning δ from θ_c. In the calculation the oscillator strength is assumed to be constant. The solid and dotted lines show the enhancement factors for p and s polarization [11,27].

density anomaly is expected since the density near the surface is confirmed to be the same as that in the bulk [25].

We show the calculated spectra by the dotted curves in Fig. 8 with the atom density of 2.15×10^{22} m^3. We have assumed here that the oscillator strength is constant. No adjustment is made in the frequency scale and the amplitude scale. Near θ_c, the agreement is satisfactory for both the s and p polarizations. However at a larger θ_i, the measured signal intensities are much larger than the calculated ones, especially for p polarization. Figure 9 is a plot that shows the ratio between the experimental and calculated $A_{s,p}(\theta_i)$. We include the uncertainty of our laser beam divergence of 0.5 mrad as expressed by the experimental uncertainties of the ratios. An increase in the relative absorption strength with increase in δ is recognized clearly.

We now take into account the electric quadrupole interaction of an atom with an evanescent field. The oscillator strength of the electric quadrupole transition depends on both the wave and the polarization vectors of the light field as shown in Eq. (6). The evanescent field has a characteristic wave vector, which is associated with the inhomogeneous nature of the field. We report in separate papers on the oscillator strength of the electric quadrupole transition in the evanescent light with its dependence on θ_i [26,27]

$$f_Q^s = \frac{k_x^2 + k_z^2}{k_0^2} f_Q = (2n_1^2 \sin^2 \theta_i - n_2^2) f_Q \equiv g_s(\theta_i) f_Q, \quad (19)$$

$$f_Q^p = \frac{4|\epsilon_x k_x|^2 + 4|\epsilon_z k_z|^2 + 3|\epsilon_x k_z|^2 + 3|\epsilon_z k_x|^2 + 10|\epsilon_x \epsilon_z k_x k_z|}{3k_0^2} f_Q$$

$$= \left(\frac{8n_1^4 \sin^4 \theta_i - 8n_1^2 n_2^2 \sin^2 \theta_i + n_2^4}{2n_1^2 \sin^2 \theta_i - n_2^2} \right) f_Q \equiv g_p(\theta_i) f_Q. \quad (20)$$

The dotted line $g_s(\theta_i)$ and the solid line $g_p(\theta_i)$ in Fig. 9 are the reproduction of the dependences for s and p polarizations, respectively. The result is in good agreement with the calculation.

Figure 9 suggests further enhancement of absorption in p polarization. However, we do not have a positive explanation at the present. A possible candidate for additional enhancement may be an effect of short-range interactions with the surface. Since the absorbing atoms are located very close to the solid surface, the absorption characteristics of the atoms could be further affected by interactions with the surface; e.g., the wave function mixing as in the case of the collision-induced dipole transition [20]. It is noted that, if the effect of the short-range interaction is substantial, the observed absorption, which is a kind of average over the evanescent light field, may be affected only by a small amount even though the effect increases with an increase in the angle of incidence.

IV. CONCLUSION

On the basis of the absorption spectroscopy on the D_2 transition of the cesium atoms we determined the oscillator strength of the cesium $6\,^2S_{1/2} \rightarrow 5\,^2D_{5/2}$ electric quadrupole transition to be $(4.69 \pm 0.05) \times 10^{-7}$. In the ATR spectra, the oscillator strengths for s and p polarizations increase with the increase in θ_i. The enhancement is reproduced by that of the oscillator strength in the evanescent light field predicted theoretically.

[1] G. M. Shrum, N. M. Carter, and H. W. Fowler, Philos. Mag. **3**, 27 (1927).
[2] K. Niemax, J. Quant. Spectrosc. Radiat. Transf. **17**, 125 (1977).
[3] V. K. Prokofíev, Z. Phys. **57**, 387 (1929); Zh. Eksp. Teor. Fiz. **1**, 123 (1931).
[4] S. M. Gridneva and G. A. Kasobov, in Proceedings of the Seventh International Conference on Phenomena in Ionized Gases, Belgrade, 1965, Vol. II, p. 581.
[5] I. V. Hertel and K. J. Ross, J. Phys. B **2**, 484 (1969).

[6] B. Sayer, R. Wang, J. C. Jeannet, and M. Sassi, J. Phys. B **4**, L20 (1971).
[7] R. J. Exton, J. Quant. Spectrosc. Radiat. Transf. **16**, 309 (1976).
[8] W. Glab and M. H. Nayfeh, Opt. Commun. **38**, 262 (1981).
[9] B. Warner, Mon. Not. R. Astron. Soc. **139**, 115 (1968).
[10] M. Weissbluth, *Atoms and Molecules* (Academic Press, San Francisco, 1978), Chap. 22, p. 497.
[11] S. Tojo, M. Hasuo, and T. Fujimoto, Phys. Rev. Lett. **92**, 053001 (2004).

[12] K. Fredriksson, H. Lundberg, and S. Svanberg, Phys. Rev. A **21**, 241 (1980).

[13] R. B. Cowan, *The Theory of Atomic Structure and Spectra* (University of California Press, Berkeley, CA, 1981), Chap. 17.9.

[14] A. Thorne, U. Litzén, and S. Johansson, *Spectrophysics* (Springer-Verlag, Berlin, 1999), Chap. 9.

[15] B. W. Shore, *The Theory of Coherent Atomic Excitation* (Wiley-Interscience, New York, 1990), Chap. 20.

[16] D. C. Morton, Astrophys. J., Suppl. Ser. **130**, 403 (2000).

[17] A. M. Akul'shin *et al.*, JETP Lett. **36**, 303 (1983).

[18] A. N. Nesmeyanov, *Vapor Pressure of Chemical Elements* (Elsevier, Amsterdam, 1963), p. 146.

[19] B. Hoeling, J. R. Yeh, T. Takekoshi, and R. J. Knize, Opt. Lett. **21**, 74 (1996).

[20] T. Fujimoto, K. Ueda, and K. Fukuda, J. Quant. Spectrosc. Radiat. Transf. **21**, 89 (1979).

[21] G. Nienhuis, F. Schuller, and M. Ducloy, Phys. Rev. A **38**, 5197 (1988).

[22] S. Tojo, M. Hasuo and T. Fujimoto, J. Phys. Soc. Jpn. **72**, 1069 (2003).

[23] P. Simoneau *et al.*, Opt. Commun. **59**, 103 (1986).

[24] S. Grafström, T. Blasberg, and D. Suter, J. Opt. Soc. Am. B **13**, 3 (1996).

[25] K. Zhao, Z. Wu, and H. M. Lai, J. Opt. Soc. Am. B **18**, 1904 (2001).

[26] The second term of $g_p(\theta_i)$ in Eq. (8) of Ref. [11] was incorrect. We give the correct expression in Eq. (20).

[27] S. Tojo and M. Hasuo, following paper, Phys. Rev. A **71**, 012508 (2005).